Phys Chem Minerals (2016) 43:707–715
DOI 10.1007/s00269-016-0827-4

ORIGINAL PAPER

Compressional behavior of omphacite to 47 GPa

Dongzhou Zhang[1] · **Yi Hu**[1,2] · **Przemyslaw K. Dera**[1,2]

Received: 29 February 2016 / Accepted: 29 June 2016 / Published online: 8 July 2016

Abstract Omphacite is an important mineral component of eclogite. Single-crystal synchrotron X-ray diffraction data on natural (Ca, Na) (Mg, Fe, Al)Si_2O_6 omphacite have been collected at the Advanced Photon Source beamlines 13-BM-C and 13-ID-D up to 47 GPa at ambient temperature. Unit cell parameter and crystal structure refinements were carried out to constrain the isothermal equation of state and compression mechanism. The third-order Birch–Murnaghan equation of state (BM3) fit of all data gives $V_0 = 423.9(3)$ Å^3, $K_{T0} = 116(2)$ GPa and $K_{T0}' = 4.3(2)$. These elastic parameters are consistent with the general trend of the diopside–jadeite join. The eight-coordinated polyhedra (M2 and M21) are the most compressible and contribute to majority of the unit cell compression, while the SiO_4 tetrahedra (Si1 and Si2) behave as rigid structural units and are the most incompressible. Axial compressibilities are determined by fitting linearized BM3 equation of state to pressure dependences of unit cell parameters. Throughout the investigated pressure range, the *b*-axis is more compressible than the *c*-axis. The axial compressibility of the *a*-axis is the largest among the three axes at 0 GPa, yet it quickly drops to the smallest at pressures above 5 GPa, which is explained by the rotation of the stiffest major compression axis toward the *a*-axis with the increase in pressure.

Keywords Pyroxene · High pressure · Single-crystal diffraction · Synchrotron · Mantle · Subduction

Introduction

Eclogite is a high-pressure mantle metamorphic rock, and it is a major constituent of the subducted slab, forming mainly from basalt or gabbro at depths greater than 40 km (corresponding to pressures greater than 1.2 GPa). Containing only minor fraction of olivine, eclogite is denser than surrounding mantle materials and provides one of the primary driving forces of the subduction process (Anderson 2007; Moghadam et al. 2010). Depending on the exact buoyancy conditions determined by the temperature profile of the subduction zone, slabs that reach to the mantle transition zone may stagnate and be subhorizontally deflected (Fukao et al. 2009; King et al. 2015; van Mierlo et al. 2013); however, in some subduction zones slabs are able to penetrate the transition zone and sink to the lower mantle (Hirose et al. 1999; van der Hilst and Karason 1999). Effects of metastable preservation of some of the upper mantle minerals including olivine and pyroxenes in the cold subduction environments on the slab buoyancy have recently been demonstrated to have significant implications for the slab stagnation (Agrusta et al. 2014; King et al. 2015; van Mierlo et al. 2013). A good understanding of the compression behavior and stability limits of mineral components of eclogite at high pressures helps to constrain the force balance of the subduction and provides valuable

Electronic supplementary material The online version of this article (doi:10.1007/s00269-016-0827-4) contains supplementary material, which is available to authorized users.

✉ Dongzhou Zhang
dzhang@hawaii.edu

[1] School of Ocean and Earth Science and Technology, Hawai'i Institute of Geophysics and Planetology, University of Hawaii at Manoa, 1680 East West Road, Honolulu, HI 96822, USA

[2] Department of Geology and Geophysics, School of Ocean and Earth Science and Technology, University of Hawaii at Manoa, 1680 East West Road, Honolulu, HI 96822, USA

information for modeling of the dynamics of subduction zones (Moghadam et al. 2010). In addition to anomalously high density, eclogite is also characterized by thermal conductivity lower than that of typical mantle harzburgite (Wang et al. 2014) and thus may serve as thermal insulating layer for the slab and control the heat flow.

Eclogites are usually composed of two major mineral phases: omphacite [(Ca, Na)(Mg, Fe, Al)Si_2O_6] and garnet (McNamara 2012; Moghadam et al. 2010). Among these two minerals, omphacite commonly serves as the framework mineral of the eclogite assembly, while garnet is dispersed in various morphologies throughout the omphacite framework (McNamara 2012). Microstructures of eclogites found at the Earth's surface show that omphacite controls the bulk rheological properties of eclogites at natural conditions (McNamara 2012; Moghadam et al. 2010). Undeformed garnet grains are usually embedded in a continuous omphacite matrix with preferred orientation (Moghadam et al. 2010). Experiments on the high-pressure behavior of natural omphacite provide therefore important information constraining the rheological behavior of eclogite at mantle conditions. Omphacite is also responsible for the low thermal conductivity of eclogite (Wang et al. 2014). In addition to eclogitic xenoliths, omphacites are often found as solid inclusions in kimberlitic diamonds (Mitchell and Giardini 1977; Promprated et al. 2004; Smyth 1980; Sobolev et al. 1999) and have been reported in chondritic meteorite samples (Kimura et al. 2013). While nominally anhydrous, natural omphacites often exhibit significant level of hydration, with OH concentrations reaching as high as 700 ppm (Koch-Muller et al. 2004, 2007), and are expected to be one of the significant water carriers into the mantle.

Depending on the crystallization conditions, omphacites can assume one of two different crystal structures: the substitutionally disordered high-temperature phase with space group *C2/c* and the cation-ordered phase with space group *P2/n* (Fleet et al. 1978; McNamara 2012; Moghadam et al. 2010; Oberti and Caporuscio 1991). At ambient pressure, the order–disorder transition takes place at 725 °C (Fleet et al. 1978). Temperature quench rate controls the diffusion-driven redistribution of cations on cooling, allowing to preserve the substitution-disordered state to ambient conditions on rapid cooling. In general, omphacites from tectonic environments, in which exhumation proceeds slowly, tend to be of the *P2/n* variety, whereas specimens from kimberlitic or meteoritic origins usually exhibit the disordered symmetry. Because of this temperature sensitivity of cation distribution, omphacites are used as a base of the omphacite–garnet geothermometer (Råheim and Green 1974). The information about exact thermoelastic properties of omphacite is also valuable for geobarometric interpretation of elastic equilibria in host–diamond–inclusion systems to constrain residual pressure and formation conditions of the inclusions (Liu et al. 1990; Zhang 1998).

From a chemical composition perspective, omphacite can be considered as an intermediate phase in diopside–jadeite solid solution system. In the chemically diverse pyroxene family, simple linear mixing models for predicting physical properties of solid solutions usually work quite well; however, in omphacite, the complicated cation ordering effects make this approach inadequate. For example, thermal conductivity (Wang et al. 2014) and single-crystal elasticity (Skelton and Walker 2015) of *P2/n* omphacite have been shown to significantly depart from the linear trends. Similar nonlinear mixing effects have been demonstrated in spodumene (Sondergeld et al. 2006), which also exhibits order–disorder polymorphism.

Omphacite like other members of the pyroxene family is not expected to be thermodynamically stable above 25 GPa; however, recent results on the kinetics of pyroxene–garnet reaction (Nishi et al. 2008; van Mierlo et al. 2013), as well as experiments confirming metastable preservation of pyroxenes to pressures as high as 50 GPa (Dera et al. 2013a; Finkelstein et al. 2015; Hu et al. 2015), at lower temperatures strongly suggest that omphacite may be present in cold subducted slabs past the mantle transition zone. Limited pressure range of both experimental and computational studies on omphacite at high pressure conducted thus far makes it difficult and unreliable to extrapolate the physical properties to these extreme conditions, particularly considering that pyroxenes are known to exhibit subtle discontinuities of their compressional behavior in the lower pressure range (Dera et al. 2013a; Finkelstein et al. 2015). To properly account for this metastable component of eclogite in geodynamic models, it is therefore important to constrain the compressional behavior of omphacite to much higher pressures. In this paper, we present results of a compressional single-crystal synchrotron X-ray diffraction study of a natural-ordered *P2/n* omphacite up to 47 GPa at ambient temperature.

Experiments

The natural (Ca,Na)(Mg,Fe,Al)Si_2O_6 omphacite sample measured in this study comes from an eclogite rock fragment found in a locality near Occidental in Sonoma County, CA, and was obtained from the University of Arizona RRUFF collection (#R061129). Electron microprobe analysis conducted at the University of Arizona determined the chemical composition of the sample as $(Ca_{0.51}Na_{0.48})(Mg_{0.44}Al_{0.44}Fe^{2+}_{0.14}Fe^{3+}_{0.02})Si_2O_6$. The composition of the sample expressed in end-member molar percentages is: $Di_{44}Jd_{44}Hd_7Ae_4Fs_1$. For simplicity, hereafter we will refer to the sample as $Di_{51}Jd_{49}$. One chip of omphacite single

crystal of about 20 μm × 20 μm × 5 μm in size was used for this experiment. The omphacite sample was first mounted onto a polymer micromesh sample holder (MiTeGen) for room pressure measurement. Then, the same crystal was loaded into a BX90 DAC (Kantor et al. 2012). The BX90 DAC maximizes the opening angle (~±30° in our case), which is preferable for the single-crystal diffraction study. Two type I diamonds with culets of 300 μm in diameter were mounted on Boehler–Almax-type WC seats. A rhenium gasket was pre-indented to ~30 μm thickness, and a 180-μm-diameter hole was drilled in the center of the pre-indention using a laser milling machine. The omphacite crystal was loaded into the center of the gasket hole, and then, the sample chamber was loaded with He as the pressure-transmitting medium using the GSECARS gas-loading system (Rivers et al. 2008). After He loading, the gasket hole shrank to about 100 μm in diameter. Throughout the whole experiment, despite gradual collapse of the gasket hole, the sample crystal stayed clear of the Re gasket edge. A few ruby spheres (~10 μm in diameter) were placed around the omphacite sample to determine the pressure in the sample chamber (Mao et al. 1986). At each pressure, ruby fluorescence spectra were taken both before and after the diffraction data collection, and the average pressure values are reported here. All the diffraction patterns were collected at ambient temperature.

Single-crystal X-ray diffraction at ambient pressure was carried out at the experimental station 13-BM-C of the Advanced Photon Source, Argonne National Laboratory. The X-ray beam was monochromated with silicon 311 crystal to 28.6 keV (0.434 A), with 1 eV bandwidth. A Kirkpatrick–Baez mirror system was used to obtain a vertical × horizontal focus spot size of 15 μm × 15 μm, measured as full width at half maximum (FWHM). The MAR165 charge-coupled device (CCD) detector (Rayonix) was placed about 175 mm away from the sample, and ambient LaB_6 powder was used to calibrate the distance and tilting of the detector. The sample was placed at the rotation center of the diffractometer and was aligned with optical microscope. A wide rotation exposure covered angular range from $\varphi = -90°$ to 90°, followed by a series of step φ-exposures, each covering 1° scan width. The typical exposure time was 1 s/°. At zero diffractometer position, the φ scan rotation axis for the 13-BM-C diffractometer is in the horizontal plane of the instrument and is perpendicular to the incident X-ray direction. After the first set of wide and step φ exposures, collected at zero detector position, similar data were recorded with the detector rotated about the horizontal axis (2θ) by 20° and then with the detector rotated about the vertical axis (ν) by 20°. The wide rotation exposures were used to extract d-spacings, azimuthal angles around the beam center, peak intensities of each diffraction peak and the step φ exposures provided the third spatial coordinate necessary for reconstructing the crystal's reciprocal lattice and were used to index the diffraction pattern.

High-pressure single-crystal X-ray diffraction images were collected at the neighboring experimental station 13-ID-D. The X-ray was monochromated to 37.0 keV (0.3344 A) with a silicon 111 crystal and then focused to 4 μm × 4 μm at the FWHM with a pair of K–B mirrors. The same MAR165 CCD detector was placed ~200 mm away from the sample in the DAC, and the detector was also calibrated with LaB_6 powder at ambient conditions. At each pressure, an ω-scan with X-ray diode was collected to determine the maximum opening angle and to determine the functional shape of the absorption effect of the diamond anvils. After the ω-scan, a wide ω exposure with typical exposure time of 1 s/° was carried to cover the maximum opening angle that the DAC allowed, followed by a series of step ω exposure, each covering 1° scan width. The ω scan rotation axis was vertical and perpendicular to the incident X-ray direction. In the 13-ID-D station, multiple detector positions were achieved by translating the detector horizontally by ±70 mm, whereas in the 13-BM-C station, a detector rotation arm was used instead. The exposure times for the wide ω rotation images were doubled when the detector was at off-center position because peaks at higher scattering angle were characterized by lower intensities.

The diffraction images were analyzed using the ATREX IDL software package (Dera et al. 2013b). Polarization, Lorentz and empirically determined diamond absorption corrections were applied to the fit peaks. The unit cell and orientation matrix were determined in RSV for each dataset. Lattice parameters were refined in RSV using a least squares fitting procedure. Changes in the sample illuminated volume and the absorption effects are corrected using the ATREX software (Görbitz 1999; Dera et al. 2013b). Corrected peak intensities were used to refine the crystal structures with SHELXL software, facilitated by WINGX and Olex2 general user interface (Dolomanov et al. 2009; Farrugia 2012; Sheldrick 2008). The crystal structure model from Mottana et al. (1979) was used as the initial model in the refinement. We used isotropic atomic displacement parameters (U_{iso}s) for all atoms. The following restraints were used in the structural refinement: (1) all structural sites were fully occupied, and the site occupancy factors were allowed to vary freely if more than one cation occupied the same site; (2) Ca^{2+} and Na^{2+} were distributed between M1 and M11, and there were no other cations occupying these two sites; (3) M2 site was only occupied by Mg^{2+} and Fe cations, and M21 site was only occupied by Al^{3+} and Fe cations; (4) Si1 and Si2 site only contained Si^{4+} cation; (5) site occupation factors for Si^{4+} and O^{2-} sites were set to 1; (6) cations which occupy the same

polyhedral site (M1, M11, M2 and M21) shared the same U_{iso} value; (7) all U_{iso} values are positive. At some pressures, the U_{iso}s of similar sites (e.g., M1/M11, M2/M21, Si1/Si2) showed strong trade-offs during fitting, and the U_{iso}s of some sites could be negative if allowed to fit freely. Given this condition, the U_{iso}s of similar sites was fitted dependently as the same value, which reduced the number of fitting parameters (supplementary materials Table 1). Refinement details, lattice parameters, fractional coordinates, atomic displacement parameters and bond lengths at different pressures are given in supplementary materials Tables 1–4. We used the VESTA software (Momma and Izumi 2008) to calculate the polyhedral volumes, average bond lengths and distortions, which are given in supplementary materials Table 5.

Results and discussions

Equation of state of omphacite

Throughout the investigated pressure range, the omphacite sample retains the *P2/n* structure. Our P–V dataset is consistent with previous studies on *P2/n* omphacite with similar compositions (Fig. 1). The isothermal bulk modulus at 0 GPa, K_{T0}, and its pressure derivative, K_{T0}', were determined by fitting the pressure–volume relation with a third-order Birch–Murnaghan equation of state (BM3) (Angel 2000). The data were fit using EoSFit 7c software (Angel et al. 2014), and the fitting was weighted by the uncertainties of both pressure and volume. The best fit gives

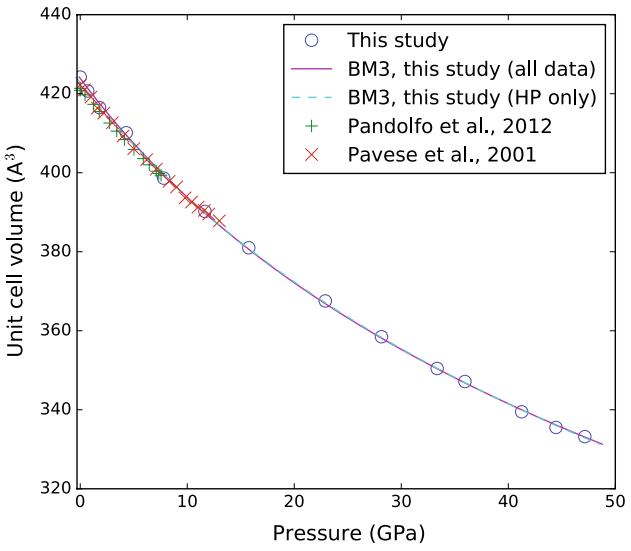

Fig. 1 Pressure dependence of unit cell volume of $Di_{51}Jd_{49}$ and the best-fit BM3 equation of state. *Error bars* are smaller than the symbols

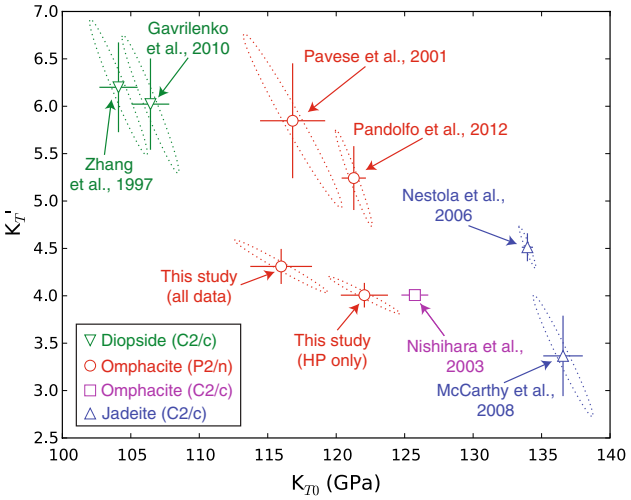

Fig. 2 Isothermal bulk moduli and their pressure derivatives of different clinopyroxenes along the diopside–jadeite join

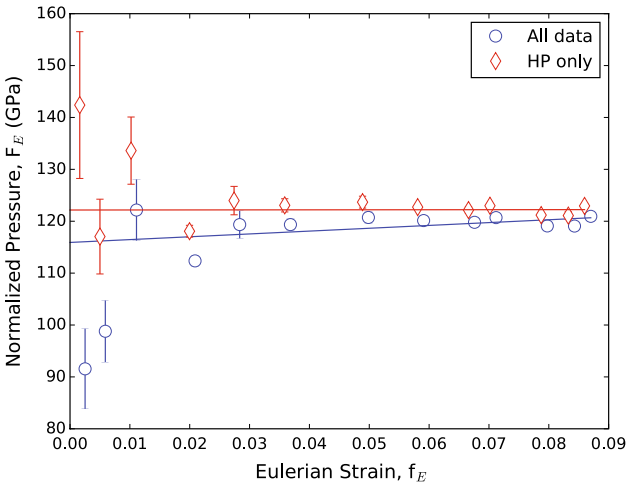

Fig. 3 f_E–F_E plots of all data (*blue circles*) and the high-pressure data only (red diamonds). *Straight lines* demonstrate the best-fit BM3 equations of state, which are weighted linear fits of the f_E–F_E datasets

$V_0 = 423.9(3)$ Å^3, $K_{T0} = 116(2)$ GPa and $K_{T0}' = 4.3(2)$. Since the ambient pressure data and the high-pressure data were collected with different instrumentations, to check whether the equation of state fitting was biased by mixing the data, we also fitted the equation of state with only the high-pressure data, which were collected with the same instrumentation. The fitting results are illustrated as "HP only" in Figs. 1, 2 and 3. Best fit of the HP only data gives $V_0 = 422.7(4)$ Å^3, $K_{T0} = 122(3)$ GPa and $K_{T0}' = 4.0(2)$. The two equations of state are nearly identical throughout the pressure range investigated (Fig. 1). On the other hand, we would like to note here that the ambient pressure data point has a better accuracy, because it does not have a limitation

of opening angle and therefore has a better coverage of diffraction peaks, so we believe that the equation of state fitted with all data should represent the compressional behavior of this omphacite sample better. In Fig. 2, we compare the bulk modulus and its pressure derivative from this study with the same quantities reported previously (Gavrilenko et al. 2010; Mccarthy et al. 2008; Nestola et al. 2006; Pandolfo et al. 2012; Pavese et al. 2001; Zhang et al. 1997). Along the diopside–jadeite join, the isothermal bulk modulus (K_{T0}) increases from ~105 GPa (diopside, Gavrilenko et al. 2010; Zhang et al. 1997) to ~135 GPa (jadeite, McCarthy et al. 2008; Nestola et al. 2006), and the K_{T0} of the *P2/n* omphacite has an intermediate value (115–122 GPa). As a reference, the ambient adiabatic bulk modulus of the *C2/c* omphacite polymorph determined by means of Brillouin spectroscopy was 130.8(5) (Bhagat et al. 1992). K_{T0}' is negatively correlated with K_{T0}. K_{T0}' decreases from ~6 (diopside, Gavrilenko et al. 2010; Zhang et al. 1997) to ~3.5 (jadeite, Mccarthy et al. 2008; Nestola et al. 2006). The K_{T0}' in this study is slightly lower than the K_{T0}' measured by previous authors, but it still follows the trends along the diopside–jadeite join. We note that our best-fit K_{T0}' is significantly smaller than the result from Pandolfo et al. (2012) (5.1 ± 0.3), though the compositions of the two samples are very similar. The potential reasons for this deviation include: (1) The diffractometer in Pandolfo et al. (2012) uses a laboratory MoKα X-ray source, whereas the synchrotron X-ray source used in this study has a higher energy, a better flux and a smaller focus, which help to improve the signal-to-noise ratio. (2) The pressure-transmitting medium used in Pandolfo et al. (2012) is methanol:ethanol:water solution, while the pressure-transmitting medium used in this study is compressed He, which is more hydrostatic and renders higher data quality at high pressures (Dera et al. 2013b).

The relationship between the normalized stress (F_E) and the Eulerian strain (f_E) gives the visual assessment of the quality of the equation of state fit (Angel 2000). The BM3 equation of state is a weighted linear fit of the f_E–F_E dataset (Angel 2000). The f_E–F_E plot for omphacite investigated in our study is shown in Fig. 3. The best-fit BM3 equations of state match most of the data, except for a few data points with very small Eulerian strain ($f_E < 0.01$), whose uncertainties are large. The f_E–F_E datasets with and without the ambient pressure data point have similar levels of scattering. The best-fit BM3 equation of state of the HP only dataset presents a nearly flat line in the f_E–F_E plot, because its K_{T0}' is 4.0(2). The HP only dataset can be fitted with a second-order Birch–Murnaghan equation of state, in which the V_0 is 422.7(3) Å^3 and the K_{T0} is 122.2(8) GPa. As we point out in earlier paragraph, the HP only dataset does not necessarily give a better representation of the compressional behavior of this specific omphacite sample, because the accessibility of the available diffraction peaks is limited at high pressures, and the ambient pressure data point should give a more accurate unit cell volume than the high-pressure data points.

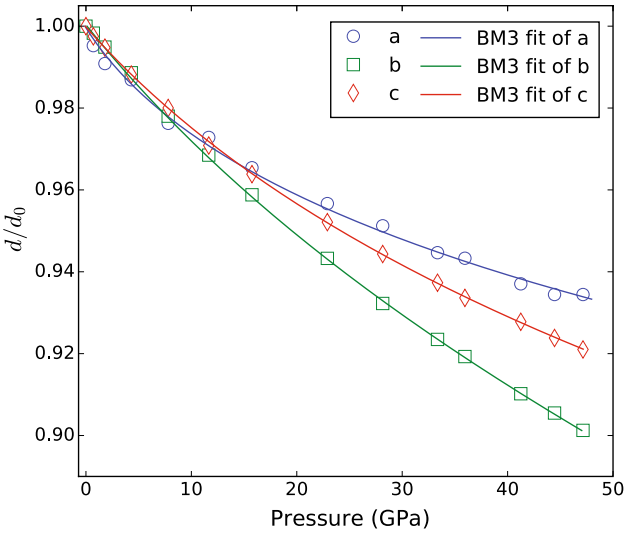

Fig. 4 Pressure dependences of normalized lattice parameters. Weighted BM3 fits of the axial compressional data are plotted in this figure

Axial compression of P2/*n* omphacite

The axial compressibilities of minerals are related to the elastic anisotropy. The axial compressibility of an axis (β) is the inverse of the axial linear modulus (Angel 2000; Hu et al. 2015; Pavese et al. 2001). We use the pressure-length BM3 equations of state to fit the lattice parameters *a, b* and *c* (Fig. 4). Then, we calculate their linear moduli from the BM3 equation of state and calculate the axial compressibilities by taking the inverse of the linear moduli. The BM3 fitting is carried out with EoSFit 7c software (Angel et al. 2014), and the fitting was weighted by the uncertainties of both pressure and volume. The best-fit BM3 parameters are listed in Table 1. We notice that the best-fit BM3 parameters of the lattice parameter *a* are very sensitive to the fitting weight assigned to each data point, yet the best-fit BM3 parameters of *b* and *c* are not sensitive to the fitting weight. This is probably because the *a*-axis has the largest error bar among the three axes, which is a result of the limited opening angle of the DAC and the orientation of the crystal. The unweighted best-fit BM3 parameters are listed in Table 1 as references. The pressure dependences of the axial compressibilities are shown in Fig. 5. We notice that the axial compressibility of the *a*-axis is the largest among the three axes at 0 GPa, yet it quickly drops to the smallest at pressures above 5 GPa. Throughout the investigated pressure range, the *b*-axis is more compressible than the *c*-axis. At 0 GPa, the anisotropy ratio

Table 1 Linear BM3 fitting parameters and axial compressibilities of the lattice parameters *a, b* and *c*

	a	*b*	*c*
d_0 (A)	**9.585(4)** *9.57(2)*	**8.7918(4)** *8.79(2)*	**5.2617(4)** *5.262(8)*
M_0 (GPa)	**244(26)** *322(46)*	**310(4)** *307(23)*	**343(4)** *343(32)*
M'	**36(6)** *25(5)*	**8.1(2)** *8.2(9)*	**12.5(3)** *13(2)*
β_0 (GPa^{-1})	**0.0041(2)** *0.0032(5)*	**0.00324(3)** *0.0033(3)*	**0.00291(2)** *0.0029(3)*

β_0 is the axial compressibility at 0 GPa. Bold values: best-fit values weighted by the uncertainties of pressure and volume. Italic values: unweighted best-fit values

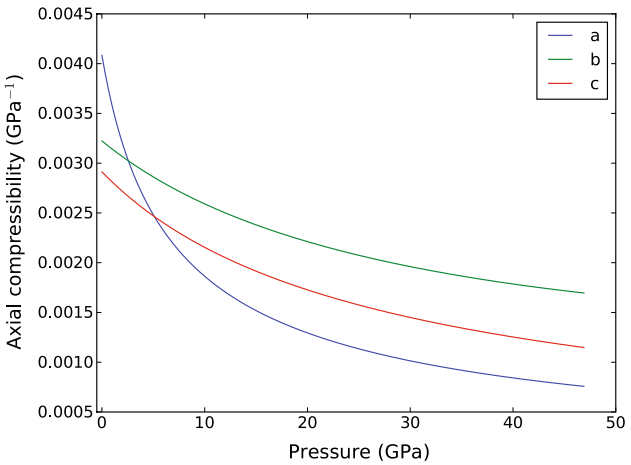

Fig. 5 Pressure dependences of the axial compressibilities. Weighted BM3 fits are used to plot this figure

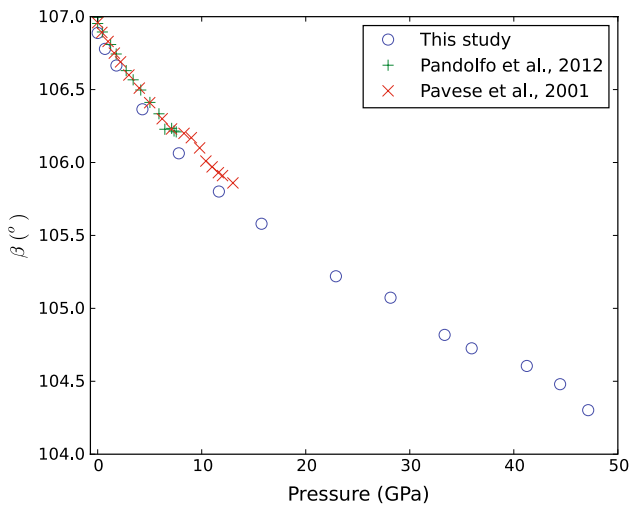

Fig. 6 Pressure dependences of the β angle of different *P2/n* omphacites

between the three axes using the weighted BM3 fitting is β_a:β_b:β_c = 1.41:1.11:1.00. The relative ratio of β_a is significantly larger than the results reported by Pandolfo et al. (2012) (β_a:β_b:β_c = 1.03:1.07:1.00) and Pavese et al. (2001) (β_a:β_b:β_c = 0.95:1.07:1.00). However, when we compare the results using the unweighted best-fit values, the anisotropy ratio changes to β_a:β_b:β_c = 1.07:1.12:1.00, which is closer to previously reported values. We note here that the *a*- and *c*-axes do not belong to the major compressional axes. The quick change of the axial compressibility of the *a*-axis is explained by the rotation of the strain tensor, which will be discussed in later sections of this manuscript.

In our unit cell setting, the β angle decreases monotonically with pressure (Fig. 6). It decreases from 106.89 ± 0.01° at 0 GPa to 104.30 ± 0.02° at 47 GPa. The decreasing trend of the β angle is consistent with previous studies on *P2/n* omphacite with similar compositions (Pandolfo et al. 2012; Pavese et al. 2001). Similar pressure dependences of the β angle are also observed in other monoclinic pyroxenes, such as diopside (Gavrilenko et al. 2010; Zhang et al. 1997), jadeite (McCarthy et al. 2008; Nestola et al. 2006) and hedenbergite (Hu et al. 2015).

Compression of polyhedra

We used two parameters to characterize the compression of each polyhedron: the polyhedron volume and the average bond length. The VESTA software was used to calculate these two parameters for each pressure point (Momma and Izumi 2008). We notice that there are some artifacts from the refinement process, which lead to trade-offs in volumes and structures between the M1/M11, M2/M21 and Si1/Si2 polyhedron pairs, so we report the average volumes and average bond lengths of octahedra (M1 and M11), eight-coordinated polyhedra (M2 and M21) and tetrahedra (Si1 and Si2), which show more smooth trends. Among the three categories of polyhedra, the eight-coordinated polyhedra show the fastest compression, while the tetrahedra show the slowest compression. The octahedra show the intermediate compression ratio, and the average octahedron compression ratio is almost identical to the compression ratio of the whole unit cell. We conclude that the compression of the eight-coordinated polyhedra contributes most to the compression of the *P2/n* omphacite. The best-fit

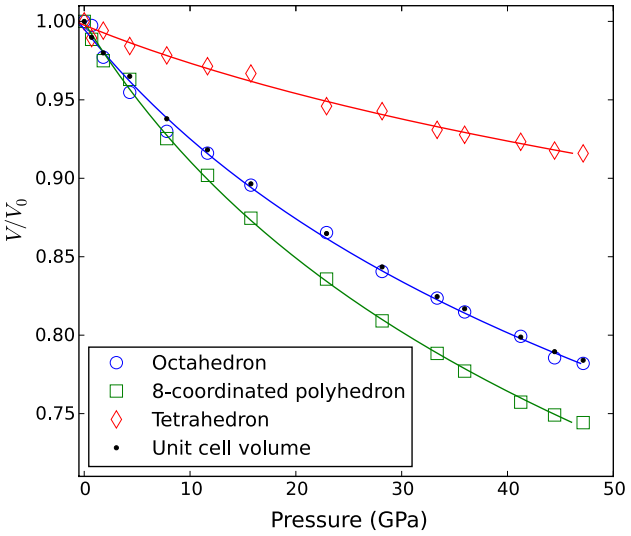

Fig. 7 Pressure dependences of average polyhedron volumes. *Blue circle* average octahedron volume (M1 and M11). *Green square* average eight-coordinated polyhedron volume (M2 and M21). *Red diamond* average tetrahedron volume (Si1 and Si2). Black dots: unit cell volume. *Blue*, *red* and *green curves* give the best fits to the BM3 equations of states

Table 2 Best-fit BM3 parameters of the average polyhedra volumes as functions of pressure

	Octahedron	Eight-coordinated polyhedron	Tetrahedron
V_0 (Å)	10.78(4)	25.48(8)	2.194(5)
K_{T0} (GPa)	118(8)	91(5)	361(5)
K_T'	4.1(5)	3.7(2)	10.0(4)

parameters of the BM3 equations of state of different polyhedra are shown in Fig. 7 and Table 2. The average bond lengths in different polyhedra show the similar behavior as the polyhedron volumes.

Strain tensor of omphacite

For a monoclinic mineral whose β angle changes with pressure, the a-axis and the c-axis of the crystal are not the directions of the minimum and maximum compressions of the crystal structure, i.e., the principle axes of the strain tensor. To fully understand the compression of the crystal under pressures, the analysis of the strain tensor as a function of pressure is needed. We use the Win_Strain program developed by Dr. Ross Angel to calculate the strain tensor of omphacite at each pressure. The mathematical notations used in the Win_Strain program are described in an earlier literature (Ohashi 1982). The eigenvalues of the strain

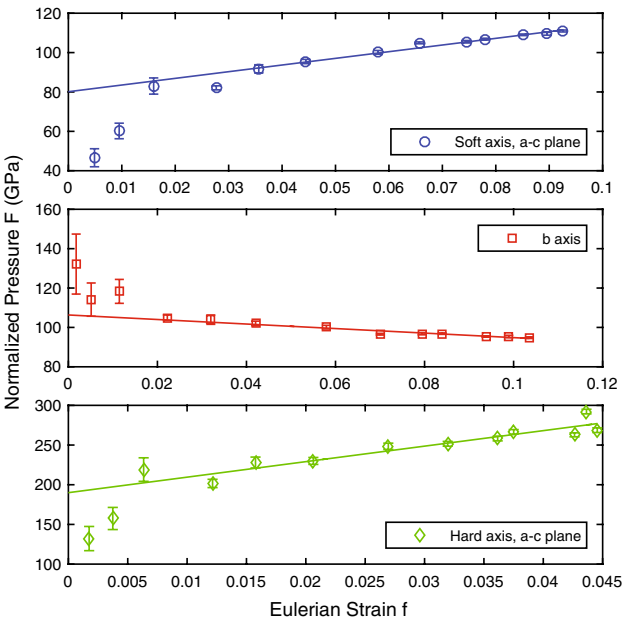

Fig. 8 f_E–F_E plot of the three major compression axes. *Straight line* indicates the weighted linear fit of each f_E–F_E plot, from which the M_0 and M′ are calculated. *Top* the "soft" major axis in the a–c plane. $M_0 = 240(16)$ GPa, $M' = 21(1)$. *Middle* the major axis along the b-axis. $M_0 = 316(8)$ GPa, $M' = 7.9(4)$. *Bottom* the "hard" major axis in the a–c plane, which is also the stiffest major axis. $M_0 = 570(85)$ GPa, $M' = 33(5)$

tensor and the directions of the major compression axes at each pressure are calculated with the Win_Strain program. One of the three major compression axes is always parallel to the b-axis of the crystal, while the other two axes are within the a–c plane. In the whole pressure range, the stiffest major axis ("hard axis") always lies in the a–c plane. The other major axis ("soft axis") in the a–c plane is the softest axis below 22.9 GPa, yet at pressures above 22.9 GPa, the b-axis becomes the softest major axis. The eigenvalues of the strain tensor give the Eulerian finite strain along the three major compression axes. By fitting the f–F plot with a linear function, it is possible to get the isothermal bulk modulus (M_0) and its pressure derivative (M') of each major compression axis (Fig. 8). With increasing pressure, the orientation of the strain tensor is rotating. To visualize the orientation of the strain tensor, we calculate the representation quadric surface of our sample at each pressure using the methodology described in Knight (2010). One major axis of the representation quadric surface is always parallel to the b-axis. In the a–c plane, the long axis of the representation quadric (the stiffest major axis) rotates toward the a-axis when the pressure goes higher (Fig. 9). The rotation of the strain tensor explains why the a-axis changes from the most compressible axis to the most incompressible axis (Fig. 5), because the stiffest

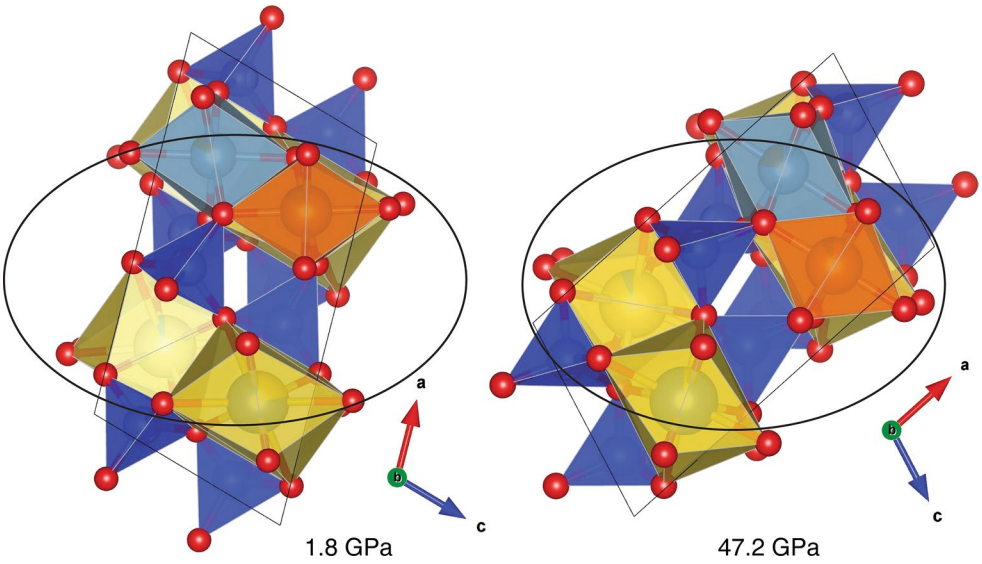

Fig. 9 Orientations of the representation quadric in the *a*–*c* plane for the isothermal compressibility tensor of omphacite at 1.8 and 47.2 GPa, viewed down *b*-axis

major compression axis rotates toward the *a*-axis with the increase in pressure.

Acknowledgments The project was supported by the National Science Foundation Division of Earth Sciences Geophysics Grant No.1344942. Development of ATREX IDL software is supported under National Science Foundation Grant No. 1440005. This work was performed at GeoSoilEnviroCARS (Sector 13), Partnership for Extreme Crystallography program (PX^2), Advanced Photon Source (APS) and Argonne National Laboratory. GeoSoilEnviroCARS is supported by the National Science Foundation—Earth Sciences (EAR-1128799) and Department of Energy—Geosciences (DE-FG02-94ER14466). PX^2 program is supported by COMPRES under NSF Cooperative Agreement EAR 11-57758. Use of the Advanced Photon Source was supported by the US Department of Energy, Office of Science, Office of Basic Energy Sciences, under Contract No. DE-C02-6CH11357. Use of the COMPRES-GSECARS gas-loading system was supported by COMPRES under NSF Cooperative Agreement EAR 11-57758 and by GSECARS through NSF grant EAR-1128799 and DOE grant DE-FG02-94ER14466. We would like to thank Prof. R. T. Downs at the University of Arizona for kindly providing the samples from RRUFF collections, Dr. R. J. Angel at the University of Padova for the helpful discussions during the 49th International School of Crystallography, the two anonymous reviewers for the very positive, thorough, and constructive comments and Dr. Milan Rieder for handling the manuscript.

References

Agrusta R, van Hunen J, Goes S (2014) The effect of metastable pyroxene on the slab dynamics. Geophys Res Lett 41:8800–8808

Anderson DL (2007) New theory of the earth. Cambridge University Press, New York

Angel RJ (2000) Equations of state. High-Temp High-Pressure Cryst Chem 41:35–59

Angel RJ, Gonzalez-Platas J, Alvaro M (2014) EosFit7c and a Fortran module (library) for equation of state calculations. Z Kristallogr 229:405–419

Baur W (1974) The geometry of polyhedral distortions. Predictive relationships for the phosphate group. Acta Crystallogr Sect B 30:1195–1215

Bhagat SS, Bass JD, Smyth JR (1992) Single-crystal elastic properties of omphacite-*C2/c* by Brillouin spectroscopy. J Geophys Res-Solid Earth 97:6843–6848

Dera P, Finkelstein GJ, Duffy TS, Downs RT, Meng Y, Prakapenka V, Tkachev S (2013a) Metastable high-pressure transformations of orthoferrosilite Fs(82). Phys Earth Planet In 221:15–21

Dera P, Zhuravlev K, Prakapenka V, Rivers ML, Finkelstein GJ, Grubor-Urosevic O, Tschauner O, Clark SM, Downs RT (2013b) High pressure single-crystal micro X-ray diffraction analysis with GSE_ADA/RSV software. High Press Res 33:466–484

Dolomanov OV, Bourhis LJ, Gildea RJ, Howard JAK, Puschmann H (2009) OLEX2: a complete structure solution, refinement and analysis program. J Appl Crystallogr 42:339–341

Farrugia LJ (2012) WinGX and ORTEP for Windows: an update. J Appl Crystallogr 45:849–854

Finkelstein GJ, Dera PK, Duffy TS (2015) Phase transitions in orthopyroxene (En(90)) to 49 GPa from single-crystal X-ray diffraction. Phys Earth Planet In 244:78–86

Fleet ME, Herzberg CT, Bancroft GM, Aldridge LP (1978) Omphacite studies; I, The *P2/n– > C2/c* transformation. Am Mineral 63:1100–1106

Fukao Y, Obayashi M, Nakakuki T, Grp DSP (2009) Stagnant slab: a review. Annu Rev Earth Pl Sci 37:19–46

Gavrilenko P, Ballaran TB, Keppler H (2010) The effect of Al and water on the compressibility of diopside. Am Mineral 95:608–616

Görbitz CH (1999) What is the best crystal size for collection of X-ray data? Refinement of the structure of glycyl-L-serine based on data from a very large crystal. Acta Crystallogr B 55:1090–1098

Hirose K, Fei YW, Ma YZ, Mao HK (1999) The fate of subducted basaltic crust in the Earth's lower mantle. Nature 397:53–56

Hu Y, Dera P, Zhuravlev K (2015) Single-crystal diffraction and Raman spectroscopy of hedenbergite up to 33 GPa. Phys Chem Miner 42:595–608

Kantor I, Prakapenka V, Kantor A, Dera P, Kurnosov A, Sinogeikin S, Dubrovinskaia N, Dubrovinsky L (2012) BX90: a new diamond

anvil cell design for X-ray diffraction and optical measurements. Rev Sci Instrum 83

Kimura M, Sugiura N, Mikouchi T, Hirajima T, Hiyagon H, Takehana Y (2013) Eclogitic clasts with omphacite and pyrope-rich garnet in the NWA 801 CR2 chondrite. Am Mineral 98:387–393

King SD, Frost DJ, Rubie DC (2015) Why cold slabs stagnate in the transition zone. Geology 43:231–234

Knight KS (2010) Analytical expressions to determine the isothermal compressibility tensor and the isobaric thermal expansion tensor for monoclinic crystals: application to determine the direction of maximum compressibility in jadeite. Phys Chem Miner 37:529–533

Koch-Muller M, Matsyuk SS, Wirth R (2004) Hydroxyl in omphacites and omphacitic clinopyroxenes of upper mantle to lower crustal origin beneath the Siberian platform. Am Mineral 89:921–931

Koch-Muller M, Abs-Wurmbach I, Rhede D, Kahlenberg V, Matsyuk S (2007) Dehydration experiments on natural omphacites: qualitative and quantitative characterization by various spectroscopic methods. Phys Chem Miner 34:663–678

Liu LG, Mernagh TP, Jaques AL (1990) A Mineralogical Raman-spectroscopy study on eclogitic garnet inclusions in diamonds from argyle. Contrib Mineral Petr 105:156–161

Mao HK, Xu J, Bell PM (1986) Calibration of the Ruby pressure gauge to 800-Kbar under quasi-hydrostatic conditions. J Geophys Res-Solid Earth 91:4673–4676

Mccarthy AC, Downs RT, Thompson RM (2008) Compressibility trends of the clinopyroxenes, and in situ high-pressure single-crystal X-ray diffraction study of jadeite. Am Mineral 93:198–209

McCormick TC, Hazen RM, Angel RJ (1989) Compressibility of omphacite to 60 kbar; role of vacancies. Am Mineral 74:1287–1292

McNamara DD (2012) Omphacite—a mineral under pressure! Geol Today 28:71–75

Mitchell RS, Giardini AA (1977) Some mineral inclusions from African and Brazilian diamonds; their nature and significance. Am Mineral 62:756–762

Moghadam RH, Trepmann CA, Stockhert B, Renner J (2010) Rheology of synthetic omphacite aggregates at high pressure and high temperature. J Petrol 51:921–945

Momma K, Izumi F (2008) VESTA: a three-dimensional visualization system for electronic and structural analysis. J Appl Crystallogr 41:653–658

Mottana A, Rossi G, Kracher A, Kurat G (1979) Violan Revisited—Mn-bearing omphacite and diopside. Tscher Miner Petrog 26:187–201

Nestola F, Ballaran TB, Liebske C, Bruno M, Tribaudino M (2006) High-pressure behaviour along the jadeite $NaAlSi_2O_6$-aegirine $NaFeSi_2O_6$ solid solution up to 10 GPa. Phys Chem Miner 33:417–425

Nishi M, Kato T, Kubo T, Kikegawa T (2008) Survival of pyropic garnet in subducting plates. Phys Earth Planet In 170:274–280

Nishihara Y, Takahashi E, Matsukage K, Kikegawa T (2003) Thermal equation of state of omphacite. Am Mineral 88:80–86

Oberti R, Caporuscio FA (1991) Crystal-chemistry of clinopyroxenes from mantle eclogites—a study of the key role of the M2 site population by means of crystal-structure refinement. Am Mineral 76:1141–1152

Ohashi Y (1982) A program to calculate the strain tensor from two sets of unit-cell parameters (STRAIN). In: Hazen RM, Finger LW (eds) Comparative crystal chemistry. Wiley, New York, pp 92–102

Pandolfo F, Nestola F, Cámara F, Domeneghetti MC (2012) High-pressure behavior of space group *P2/n* omphacite. Am Mineral 97:407–414

Pavese A, Diella V, Levy D, Hanfland M (2001) Synchrotron X-ray powder diffraction study of natural P2/n-omphacites at high-pressure conditions. Phys Chem Miner 28:9–16

Promprated P, Taylor LA, Anand M, Floss C, Sobolev NV, Pokhilenko NP (2004) Multiple-mineral inclusions in diamonds from the Snap Lake/King Lake kimberlite dike, Slave craton, Canada: a trace-element perspective. Lithos 77:69–81

Råheim A, Green D (1974) Experimental determination of the temperature and pressure dependence of the Fe–Mg partition coefficient for coexisting garnet and clinopyroxene. Contrib Mineral Petr 48:179–203

Rivers M, Prakapenka VB, Kubo A, Pullins C, Holl CM, Jacobsen SD (2008) The COMPRES/GSECARS gas-loading system for diamond anvil cells at the Advanced Photon Source. High Press Res 28:273–292

Robinson K, Gibbs GV, Ribbe PH (1971) Quadratic elongation: a quantitative measure of distortion in coordination polyhedra. Science 172:567–570

Sheldrick GM (2008) A short history of SHELX. Acta Crystallogr A 64:112–122

Skelton R, Walker AM (2015) The effect of cation order on the elasticity of omphacite from atomistic calculations. Phys Chem Miner 42:677–691

Smyth JR (1980) Cation vacancies and the crystal-chemistry of breakdown reactions in kimberlitic omphacites. Am Mineral 65:1185–1191

Sobolev VN, McCammon CA, Taylor LA, Snyder GA, Sobolev NV (1999) Precise Mossbauer milliprobe determination of ferric iron in rock-forming minerals and limitations of electron microprobe analysis. Am Mineral 84:78–85

Sondergeld P, Li BS, Schreuer J, Carpenter MA (2006) Discontinuous evolution of single-crystal elastic constants as a function of pressure through the C2/c <–> P2(1)/c phase transition in spodumene (LiAlSi2O6). J Geophys Res-Solid Earth 111:B07202

van der Hilst RD, Karason H (1999) Compositional heterogeneity in the bottom 1000 kilometers of Earth's mantle: toward a hybrid convection model. Science 283:1885–1888

van Mierlo WL, Langenhorst F, Frost DJ, Rubie DC (2013) Stagnation of subducting slabs in the transition zone due to slow diffusion in majoritic garnet. Nat Geosci 6:400–403

Wang C, Yoneda A, Osako M, Ito E, Yoshino T, Jin ZM (2014) Measurement of thermal conductivity of omphacite, jadeite, and diopside up to 14 GPa and 1000 K: implication for the role of eclogite in subduction slab. J Geophys Res-Solid Earth 119:6277–6287

Zhang YX (1998) Mechanical and phase equilibria in inclusion-host systems. Earth Planet Sci Lett 157:209–222

Zhang L, Ahsbahs H, Hafner SS, Kutoglu A (1997) Single-crystal compression and crystal structure of clinopyroxene up to 10 GPa. Am Mineral 82:245–258